Image Deep Learning Assisted Prediction of Mechanical and Corrosion Behavior for Al-Zn-Mg Alloys

MIN AO [1], YUCHENG JI[1], XIAOGUANG SUN [2], FENGJIA GUO[3], KUI XIAO[1], AND CHAOFANG DONG [1]

[1] Key Laboratory for Corrosion and Protection (MOE), Beijing Advanced Innovation Center for Materials Genome Engineering, Institute for Advanced Materials and Technology, University of Science and Technology Beijing, Beijing 100083, China
[2] Technical Engineering Department, CRRC Qingdao Sifang Company Ltd., Qingdao 266111, China
[3] Shandong Nanshan Aluminium Company Ltd., Longkou 265706, China

Corresponding author: Chaofang Dong (cfdong@ustb.edu.cn)

ABSTRACT The use of metallographic images to predict the mechanical properties of materials and their corrosion behavior is helpful in achieving nondestructive detection and quality control. However, after a long-term attempt, the traditional methods cannot accurately correlate the mechanical properties and corrosion behavior of materials with the corresponding microstructure images. In this study, we propose a deep learning strategy to predict the mechanical property and corrosion behavior of large-scale extruded aluminum profiles using surface optical microstructure images. The proposed models with remarkable properties were established through experimental dataset collection, dataset preprocessing, deep learning network modification, and key parameter screening. Taking extruded Al-Zn-Mg alloys with different surface microstructures as example materials, 4,800 sets of ''metallographic image – hardness (HV) – corrosion potential (E_{corr})'' data were experimentally collected to establish the HV and E_{corr} models with prediction accuracies of 90% and 82%, respectively. The proposed HV and E_{corr} models exhibit great generalization ability with mean average errors of 1.8 HV and 7.0 mV on experimental validation sets, respectively. The proposed model can accurately correlate the metallographic images, mechanical property, and corrosion behavior, which can provide theoretical support for intelligent and nondestructive testing methods to further prevent unexpected material failure.

INDEX TERMS Deep learning, aluminum extrusion, mechanical property, corrosion behavior.

I. INTRODUCTION

Extruded aluminum alloys are one of the most widely used structural materials in the construction of high-speed rail systems owing to their high strength [1], low density [2], and other outstanding properties [3]. Extrusion is a complex deformation process involving a highly uneven strain and temperature distribution [4], which induces a heterogeneous microstructure in aluminum profiles [5]. Furthermore, alteration of alloy properties by the microstructure significantly affects the long-term durability of the key load-bearing

The associate editor coordinating the review of this manuscript and approving it for publication was Szidonia Lefkovits [.]

component of high-speed trains and becomes a significant problem [6], [7].

The inhomogeneous microstructure of the extruded aluminum is attributed to the degree of completeness of recrystallization from the center to the surface region of the profiles during the extrusion process [8]–[10]. Sun *et al.* reported that recrystallization should satisfy the critical conditions of high temperatures (450-550 °C) and large strain (>1) [11]. Geertruyden *et al.* summarized that the strain of the aluminum extrusion surface could reach 6 during hot deformation, which completely satisfies the critical conditions for recrystallization [12]. Therefore, recrystallization of the surface region of the extruded aluminum alloy commonly occurs

and is hardly avoided [13]–[16]. Even so, researchers are still attempting to control the microstructure of extrusion via efficient changes in the extrusion parameters and aluminum compositions [17]–[19]. However, the quality and stability of the extruded products cannot be fully guaranteed owing to the narrow process window and various influencing factors in the production cycle [20]. Moreover, the mechanical and corrosive property changes induced by recrystallization have been studied by many researchers. The mechanical properties of the profiles were significantly deteriorated by surface recrystallization [21]–[23]. However, Ye *et al.* indicated that the softening effect no longer exists when the thickness of the surface recrystallization layer is less than 200 μm [24]. In addition, Zhang *et al.* indicated that the recrystallized region of aluminum alloys exhibits low corrosion susceptivity than other region [25]. Wloka *et al.* demonstrated that a 30 μm thick recrystallized surface layer of Al-Zn-Mg alloy showed better exfoliation corrosion resistance than the matrix [26]. Our previous work also indicated that the 25 μm thick surface recrystallization layer reduced the stress corrosion cracking (SCC) susceptibility of Al-Zn-Mg alloy extrusion without sacrificing mechanical properties [27]. The surface recrystallization is often appearing as coarse or fine equiaxed grain which different from the deformed region of materials. It is noteworthy that the correlation of microstructure and properties is commonly described by data statistics methods in the literature and many similar studies [28], such as correlating the properties and average grain size [29]. However, these statistical results cannot comprehensively represent the grain structure characteristics of materials, especially deformed grain structures. To address these limitations, computer vision techniques, particularly deep learning methods, have been employed to compensate for this deficiency.

Since AlexNet was first presented in the ImageNet Large-Scale Visual Recognition Competition (ILSVRC) [30], more deep neural networks have been proposed, and innovations in deep learning continue to result in breakthroughs across multiple fields. Dong *et al.* first proposed the use of deep convolutional neural networks (CNNs) to learn the end-to-end mapping relationship between low- and high-resolution images for image recognition [31]. Deep learning has since been successfully used in the field of image recognition. More recently, literature has emerged that suggests the accurate diagnosis of diseases, particularly breast cancer, chronic kidney disease, and dermatosis, with the assistance of deep learning networks such as the Visual Geometry Group network (VGG Net) [32], GoogLeNet [33], deep residual network (ResNet) [34], faster R-CNN network [35], densely connected networks (DenseNet) [36], generative adversarial networks (GANs) [37], and Inception-ResNet networks [38]. In addition, deep learning has been applied in materials science and has achieved favorable results [39], [40]. Ma *et al.* developed a novel transfer learning strategy to address the problems of small or insufficient microstructure data using a GAN framework [41]. Na *et al.* proposed
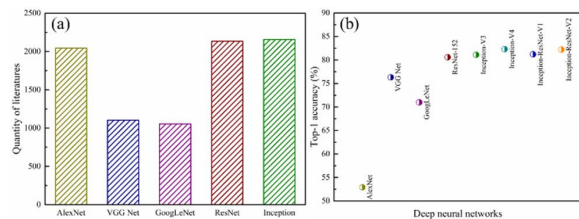

FIGURE 1. (a) Quantity of literatures in topic of different network from web of science in recent 5 years (2020-2016); (b) Top-1 accuracy of each network in ILSVRC.

a deep-learning-based method that can refocus low-quality scanning electron microscopy (SEM) images and perform the task discriminately [42]. Fig. 1(a) summarizes the quantity of literature on AlexNet, VGGNet, GoogLeNet, ResNet, and Inception networks in the last five years (2020–2016). ResNet and Inception are the most popular networks in published literature. Fig. 1(b) summarizes the top-1 accuracy of the above-mentioned networks on the ImageNet database [43]–[47]. Inception-V4 and Inception-ResNet-V2 networks exhibited better performance than the others.

In this study, we address the topic of correlation between microstructure and properties for a model Al-Zn-Mg alloy extrusion and propose a deep learning framework that can accurately predict the mechanical property and corrosion performance of aluminum extrusion via surface metallographic images. The microstructure differences, corresponding mechanical property, and corrosion behavior were studied using electron backscatter diffraction (EBSD), SEM, transmission electron microscopy (TEM), hardness testing, and electrochemical tests. Furthermore, a deep learning model was established using efficient training and appropriate parameters. The results could potentially provide theoretical support for nondestructive testing of large-scale extruded profiles.

II. METHODS
A. IMAGE-PERFORMANCE PREDICTION FRAMEWORK
In this study, the prediction strategy of "data collection $\rightarrow$ data preprocessing $\rightarrow$ deep learning modeling $\rightarrow$ correlation model accomplishment" was used to rationally and efficiently compensate for the direct correlation of metallographic images, mechanical property, and corrosion behavior of large-scale extruded sections. The flowchart of the framework is shown in Fig. 2.

1) DATA COLLECTION
We collected the "metallographic image – hardness (HV) – corrosion potential (E_{corr})" data of different extruded aluminum surface through experimental measurements. The data collection process is illustrated in Fig. 3. Three-meter length hollow aluminum profiles with different surface conditions were chosen for this study, as shown in Fig. 3(a). To comprehensively obtain the surface characteristics, the samples used for data collection were taken from the
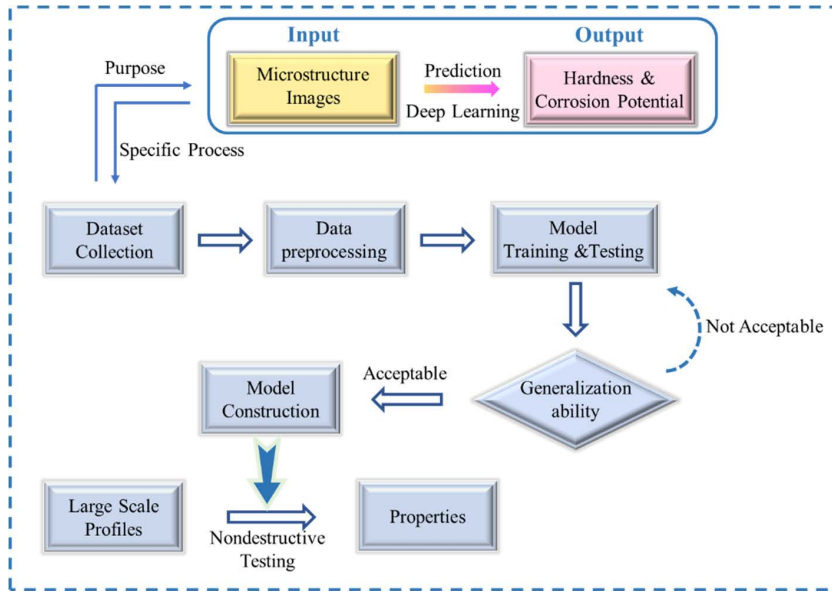
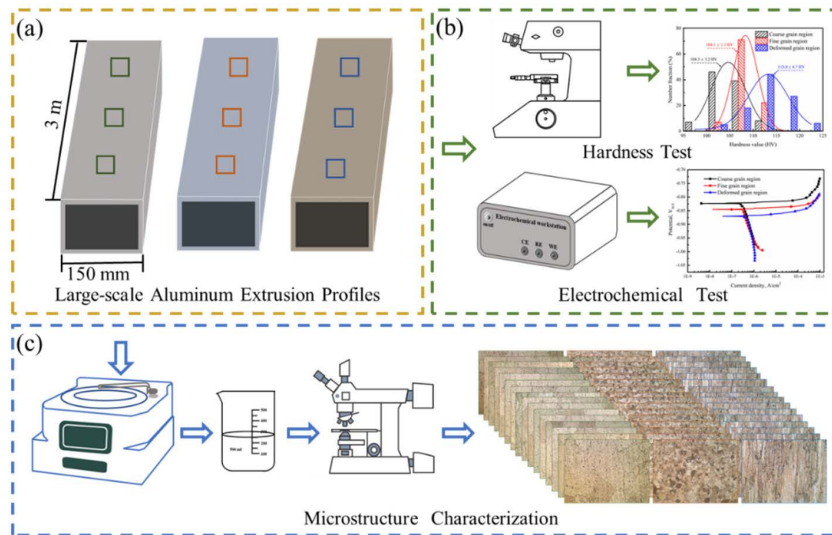**FIGURE 2.** Framework flow chart of this work.

FIGURE 3. The technological process of dataset collection (a) large-scale extruded aluminum; (b) HV and E_{corr} data collection; (c) metallographic image collection.

head, middle, and tail of the extruded profile. The input images (323×242 pixels) represented the surface optical microstructure of each extruded profile. The steps are shown in Fig. 3(c). The outputs were the surface HV and E_{corr}. The microstructure and the corresponding HV and E_{corr} showed a strict one-to-one correlation. Finally, 4,800 sets of "metallographic image – HV – E_{corr}" data were collected through experiments.

2) DATA PREPROCESSING
To prevent overfitting, the input metallographic image data were preprocessed using particular operations, including mirroring, rotation, Gaussian noise, and size changes at random.

The output HV and E_{corr} data were normalized to accelerate the optimization process of the deep learning model.

3) DEEP LEARNING MODELING
This study used Google's Inception-ResNet-V2 network with 152 convolution layers to establish the deep learning prediction model, which yielded an excellent performance. The network architecture is shown in Fig. 4. The aim of this work was to model a regression problem. Therefore, the last fully connected layer was altered to one node to accomplish the regression task. The CNN layers were applied using the ReLU activation function. Mean squared error (MSE) loss was used as an objective function for the regression
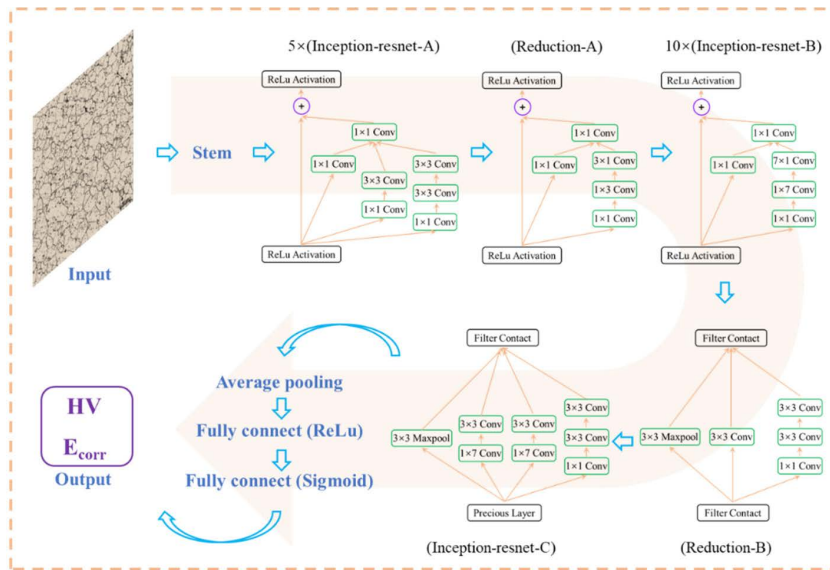
FIGURE 4. Architecture of Inception-ResNet V2.

tasks to predict continuous values. Training of the models was performed in batches of 16 images for 30 epochs with different learning rates. The training was performed using the Adam optimizer, with a weight decay of 10^{-4}. The dropout rate was set at 0.5. The models were implemented using PyCharm software. No samples overlapped between the training and testing sets.

B. EVALUATION METRICS OF MODEL

In this study, prediction accuracy and mean average error (MAE) were employed to evaluate the applicability and superiority of the framework. Fig. 5 shows the HV and E_{corr} data distributions of each extruded profile. For idealized materials with uniform microstructures, HV and E_{corr} do not change with the testing locations. The datasets used in this study comprised experimental data of engineering materials that went through the entire production cycle. Hence, the databases were heavily affected by experimental noise, testing equipment errors, and heterogeneity of materials. In most practical applications and published literature, the HV and E_{corr} were determined within an error range. To address this, thresholds must be set to define the acceptable deviation ranges. Thus far, many researchers have manually determined the appropriate tolerance parameters for their specific dataset [48]. Samples A, B, and C possess average hardness of 104.5 ± 3.2 HV, 108.1 ± 2.3 HV, and 113.0 ± 4.7 HV, respectively, and average corrosion potentials of -830.13 ± 11.86 mV, -843.98 ± 6.32 mV, and -877.49 ± 10.40 mV, respectively. Hence, error bounds of ± 3 HV for HV predictions and ± 10 mV for E_{corr} predictions were set for the prediction accuracy calculation. The prediction accuracy expresses the fraction of images that are correctly predicted from all images in the dataset.

The corresponding equations are as follows:

$$\text{Prediction accuracy} = \frac{m_{correct}}{n} \times 100\% \qquad (1)$$

where $m_{correct}$ represents the quantity of images that are correctly predicted, and n is the quantity of all images in the dataset.

The MAE was calculated using the following equation:

$$MAE = \frac{1}{n} \sum \left| \left(x_{\exp eriment} - x_{prediction} \right) \right| \qquad (2)$$

where $x_{prediction}$ represents the predicted properties, $x_{experiment}$ denotes the measured properties, and n is the quantity of data in the dataset.

C. EXPERIMENTAL PROCEDURES

This study employed extruded Al-Zn-Mg alloys in the T5 condition. The chemical compositions of these alloys are listed in Table 1. Owing to the different extrusion parameters, the surfaces of the extruded profiles exhibited different microstructural characteristics. The samples for the microstructure analysis, hardness test, and electrochemical measurements were cut from the outermost surface of each extruded aluminum profile.

TABLE 1. Chemical composition of the employed Al-Zn-Mg alloys.

Element	Al	Zn	Mg	Mn	Cr	Fe	Cu	Si
Content (wt.%)	Bal.	4.38	1.04	0.37	0.23	0.18	0.16	0.07

Metallurgical microscope (Carl Zeiss Axio Scope A1) was used to analyze the optical microstructures of the tested samples and capture the metallographic images of dataset. The conventional polished samples were corroded by aqueous acid solutions (2.5% HNO_3 and 1.5% HCl,
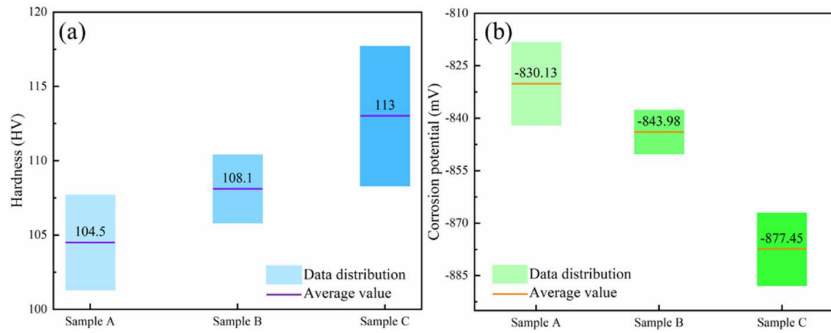
FIGURE 5. Data distribution (a) HV; (b) E_{corr}.

1% HF, and 95% H_2O by volume fraction) for 20 s and cleaned by ethanol solution for microstructure analyses. EBSD (Tescan mira 3 LMH) measurements were employed to obtain the microstructure characteristic of the tested samples. The EBSD samples were mechanically polished and then electropolished at a DC voltage of 18 V for 30 s. SEM (S-3400N, Hitachi, Japan) and energy-dispersive X-ray spectroscopy (EDS) were performed on mechanical polished surface to analyze the morphology and chemical composition of the tested samples. TEM (FEI Tecnai G20) samples were cut and polished to a size of $\Phi 3$ mm $\times$ 30 μm, and finally ion beam thinned. A Vickers hardness tester was used to calculate the hardness value for extruded aluminum with a load of 0.98 N held for 30 s.

Potentiodynamic polarization measurements were measured in a 3.5 wt.% NaCl solution by a three-electrode electrochemical (CS electrochemical workstation). A platinum plate and saturated calomel electrode (SCE) were functioned as the counter electrode and reference electrode, respectively. The working electrode was the tested samples (10 mm $\times$ 10 mm $\times$ 3 mm) that was connected to a copper wire via welding and subsequently embedded in an epoxy resin. The samples were then polished to a mirror finish and cleaned using distilled water and ethanol. The air-formed oxide film on the samples were removed by polarization. All tested samples were immersed in the 3.5 wt.% NaCl solution to reach the steady open circuit potential (OCP). The potentiodynamic polarization measurements were conducted at a scanning rate of 0.1667 mV/s. All measurements were performed at room temperature (25 °C $\pm$ 2 °C).

III. RESULTS

A. DATASET CHARACTER

The "metallographic image – HV – E_{corr}" data of three extruded aluminum with different surface microstructures were collected through experimental measurements. The surface microstructure characteristics of each profile and quantity of data are listed in Table 2. To inspect samples in a fast, nondestructive, and easy-to-execute manner, optical microstructures were chosen as the input parameters. The clear grain size characteristics obtained from the optical

TABLE 2. The surface microstructure character of each aluminum profiles and the number of samples in dataset.

Sample code	A	B	C
Average grain size (μm) (length × width)	123 × 116	16 × 21	15 × 61
Quantity (set)	1600	1600	1600

microstructure indicated a significant difference in the grain size of the extruded aluminum. Therefore, we established a dataset with 4,800 sets of data, that is, 1,600 sets of data for each sample.

B. KEY PARAMETERS SETTING AND MODELING

Based on the surface microstructure characteristics of the extruded aluminum and the corresponding HV and E_{corr}, a prediction model was established to correlate the metallographic images and properties with the assistance of the Inception-ResNet-V2 network. The HV data represent the mechanical property of the extruded aluminum. The E_{corr} data from potentiodynamic polarization represent the corrosion behavior. The total loss was used as an indicator to evaluate the convergence and fitting effects of the training processes. The total loss is a non-negative real-value function used to estimate the inconsistency between the predicted and real values of the model. The smaller the loss function, the greater is the robustness of the model. First, the models were trained using 0.00001, 0.000001, and dynamic learning rates. Fig. 6 shows the loss function alteration of the prediction model with the different learning rates. The training loss was stable and converged after 3,000 training iterations. The ranking in terms of total loss, from the lowest to highest, was the dynamic learning rate, 0.000001 learning rate, and 0.00001 learning rate. The prediction accuracy of each model stabilized after 4,000 iterations, and the MAE stabilized in the last 1,000 iterations. The dynamic learning rate outperformed the other learning rates in the training dataset, exhibiting the highest prediction accuracy and lowest MAE for both the HV and E_{corr} models.

The prediction accuracy of the established model for different training datasets is shown in Fig. 7. With the
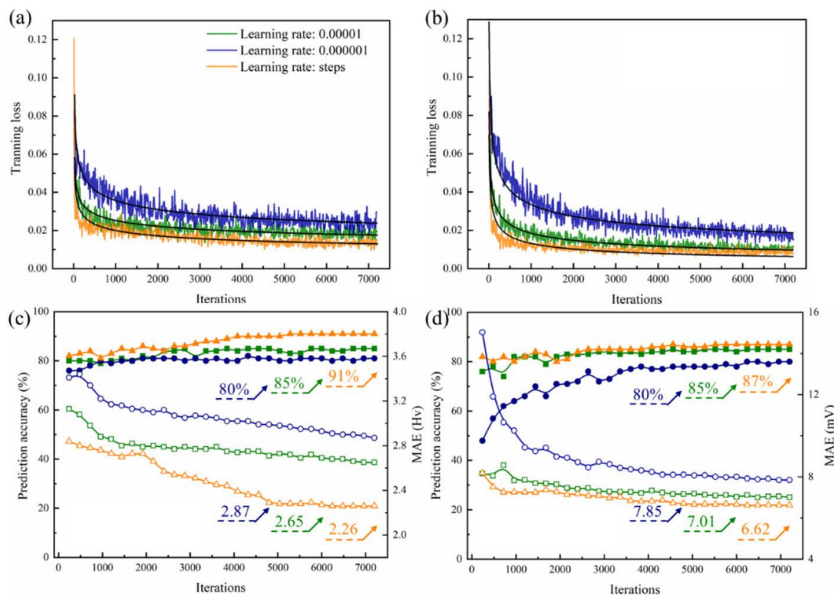
FIGURE 6. The performance of prediction model with different learning rate (a) the training loss of HV model; (b) the training loss of E_{corr} model; (c) the training performance of HV model; (d) the training performance of E_{corr} model.
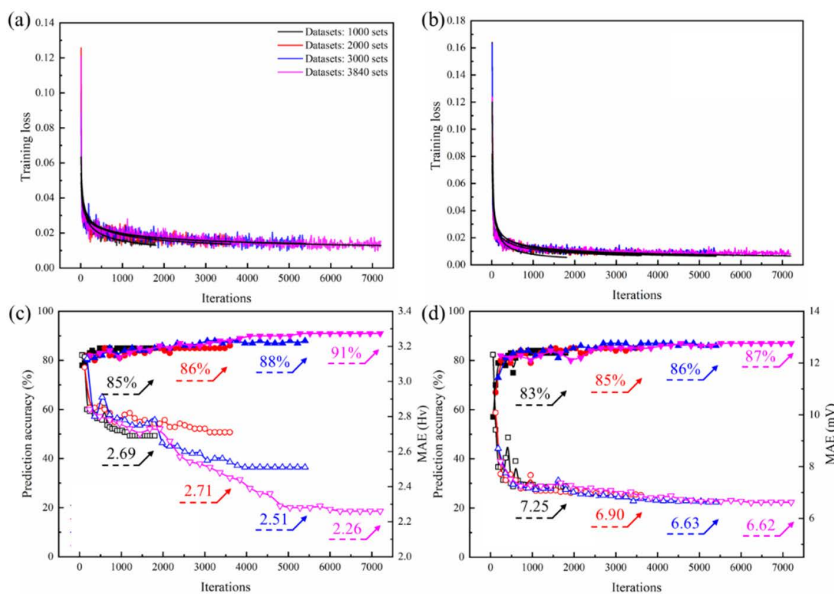

FIGURE 7. The performance of prediction model with different quantity of datasets (a) the training loss of HV model; (b) the training loss of E_{corr} model; (c) the training performance of HV model; (d) the training performance of E_{corr} model.

increase in the dataset quantity, the total loss of each model decreased and became stable after 4,000 iterations. The HV and E_{corr} models had higher prediction accuracy and lower MAE when the training datasets included at least 3,840 sets of data. Furthermore, 960 sets of testing data were used to test the performance of each model, as shown in Fig. 8. The results indicated that the HV and E_{corr} models performed well on the testing datasets. The established HV and E_{corr} models exhibited high prediction accuracies of 90% and 82%, respectively. The MAE values of the HV and E_{corr} models were 2.26 HV and 6.62 mV, respectively.

C. EXPERIMENTAL VERIFICATION

To further verify the performance of the established model and demonstrate its general applicability to other extruded aluminum alloys, we collected 30 sets of data on the surface of the extruded aluminum, and the results are displayed
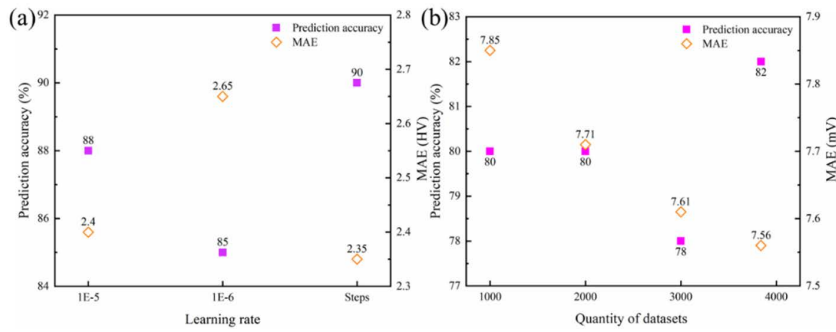
FIGURE 8. The performance of (a) HV model; (b) E$_{corr}$ model on testing datasets.
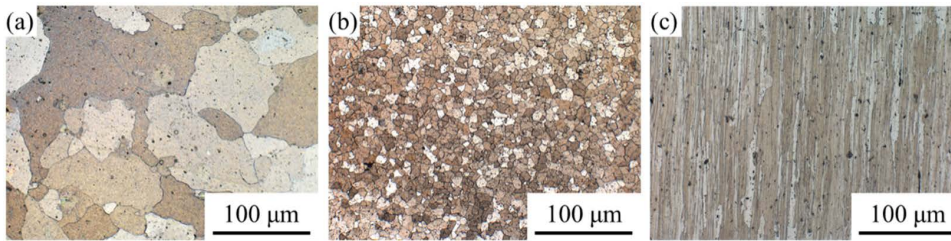

FIGURE 9. The representative metallographic image for model verification (a) sample α; (b) sample β; (c) sample γ.

TABLE 3. Surface microstructure character of verification aluminum profiles and the number of samples.

Sample code	α	β	γ
Average Grain size (μm) (length $\times$ width)	101 $\times$ 94 (coarse gains) 22 $\times$ 16 (fine grains)	24 $\times$ 21	15 $\times$ 93
Quantity (set)	10	10	10

in Fig. 9. Table 3 summarizes the grain size characteristics of the samples used for verification. The average grain size of sample α was mostly 100 μm, and a minority had an average grain size of 20 μm. Fig. 9(a) shows that the smaller grains are distributed like islands among the larger grains. The average grain size of sample β was 23 μm, and the average width of the fiber grain in sample γ was 15 μm. The microstructure images used for verification were different from the established "metallographic image – HV – E$_{corr}$" dataset to verify the generalization ability of the proposed model accurately.

The verification results are shown in Fig. 10. The results showed that compared with the discrete characteristics of the experimental value, the predicted value showed convergence properties for each surface. The established model can accurately predict the HV and E$_{corr}$ of each sample from optical microstructure images. The predicted values were mostly within the error bounds. The MAE values of the HV and E$_{corr}$ models were 1.8 HV and 7.0 mV, respectively.

IV. DISCUSSION

A. RELATIONSHIPS BETWEEN MICROSTRUCTURE AND CORRESPONDING PROPERTIES

The surface morphology of the extruded aluminum was strongly influenced by temperature and strain alteration during the extrusion process. Furthermore, the surface morphology significantly affected the mechanical properties and corrosion behavior of the aluminum extrusion. To comprehensively understand the relationship between the microstructure and properties, the microstructural characteristics of samples α, β, and γ were studied in detail. First, the surface microstructure of each extruded aluminum sample was studied, as shown in the EBSD maps (Fig. 11). The extrusion process has an apparent influence on the grain size and morphology. It can be seen intuitively that samples α, β, and γ possessed coarse equiaxed grains with an average diameter of 100 $\pm$ 5 μm, fine grains with an average diameter of 15 $\pm$ 5 μm, and deformed grains with an average width of 20 $\pm$ 5 μm, respectively. The EBSD results also indicate that sample α was completely recrystallized and released the residual stress. Sample β was in an almost completely recrystallized state with less residual stress, whereas sample γ was in a deformed state with high residual stress. The recrystallization process can release the residual stress of materials induced by the deformation process and further induce softening of the materials [49]. The microstructure features of extruded aluminum in Fig. 11 are consistent with those in the relevant published paper [50].
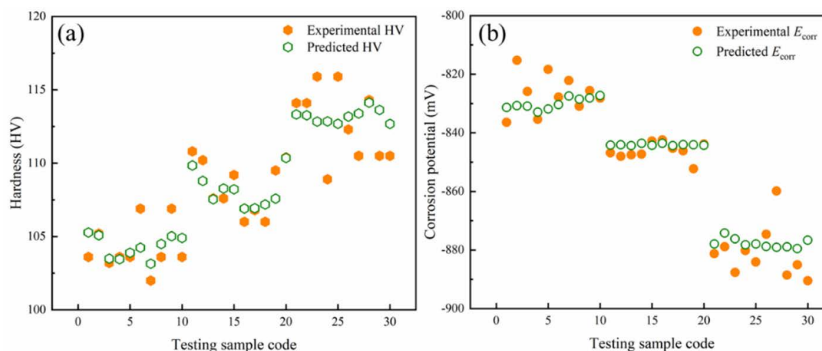
FIGURE 10. The performance of prediction model (a) HV model; (b) E_{corr} model.
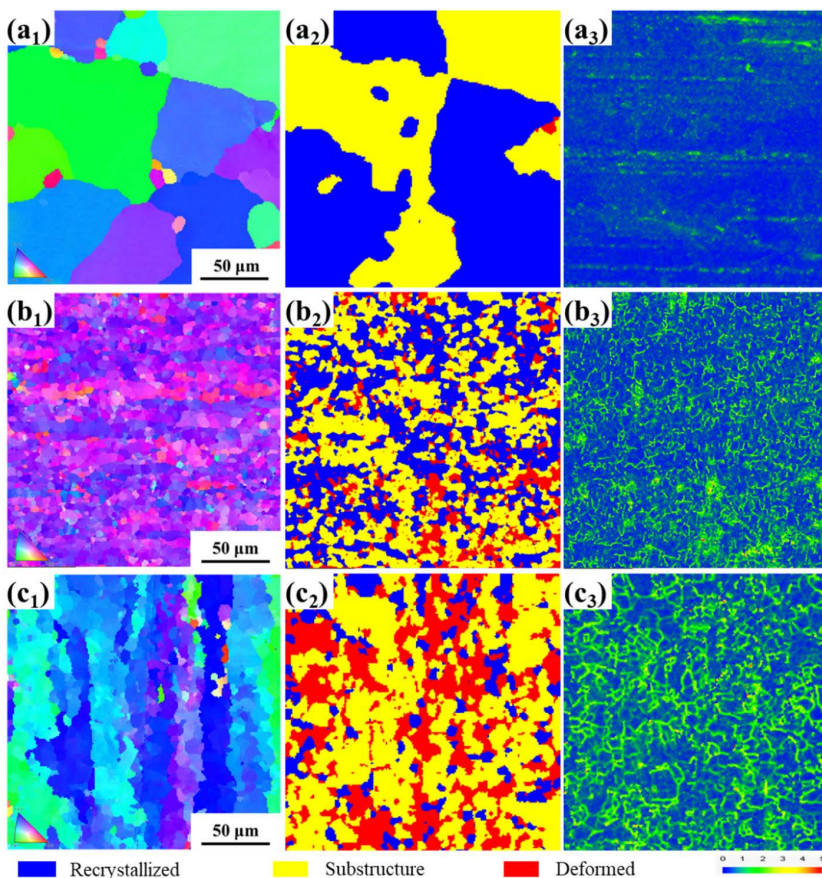

FIGURE 11. The microstructure of each extruded Al-Zn-Mg alloy (a) sample α; (b) sample β; (c) sample γ.

The uneven strain and temperature distributions during the extrusion process also have an obvious influence on the intermetallic particles (IMPs) in the aluminum profiles [51]. First, micron-scale IMPs were studied, as shown in Fig. 12. The SEM and EDS results of each sample showed that the IMPs primarily consisted of Al, Si, Mn, and Fe, that is, the AlFeMnSi phase. The IMPs in each sample exhibited obvious differences in numbers, as shown in Fig. 12(d). The area fractions of the IMPs in each sample were 0.49% ± 0.03%,

0.61% ± 0.11%, and 1.10% ± 0.25%, respectively. During the recrystallization process, the IMPs dissolved because of the relatively high temperature and then re-precipitated during the subsequent cooling process [52]. According to Montheillet *et al.*, the surface of extruded aluminum is more susceptible to high temperatures and strain than the inner region [53]. Hence, the number of IMPs decreased in the thickness direction from the surface to the inner region of the extruded aluminum.
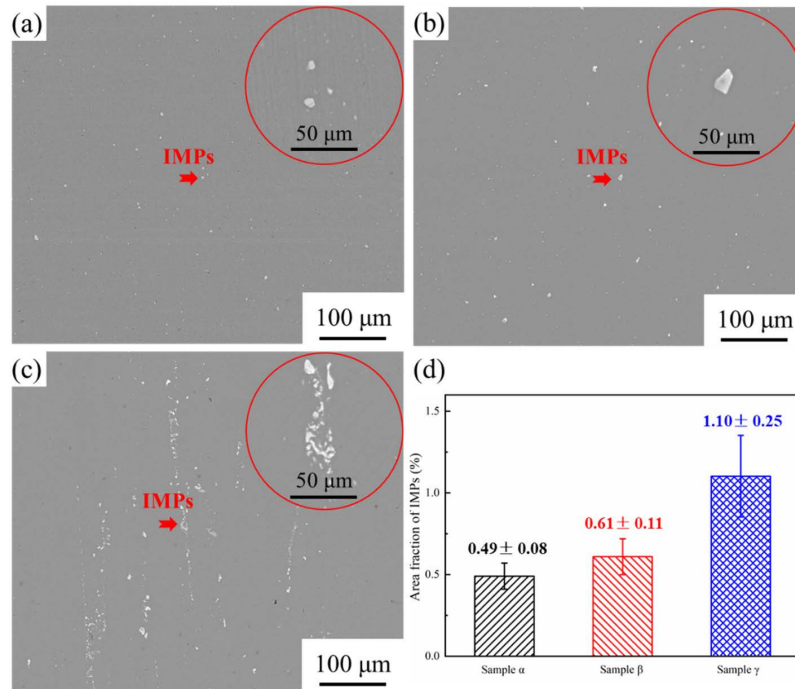
FIGURE 12. SEM image and related EDS results of IMPs in each sample (a) sample α; (b) sample β; (c) sample γ; (d) area fraction of IMPs.
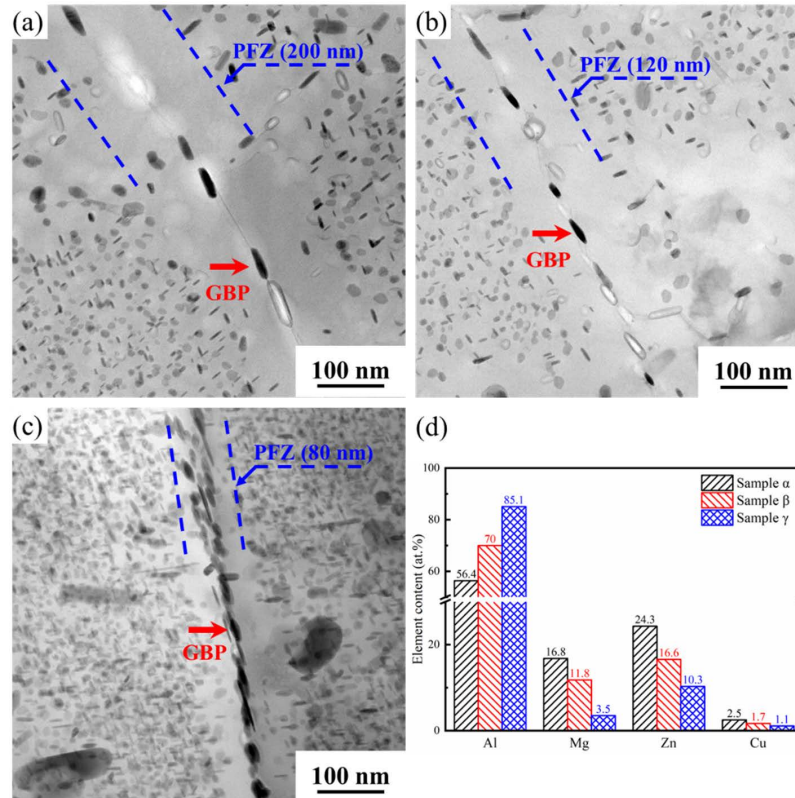
FIGURE 13. TEM micrographs of the grain boundaries of each extruded Al-Zn-Mg alloy (a) sample α; (b) sample β; (c) sample γ; (d) chemical composition of GBPs.

In addition, the nanoscale precipitates were influenced by recrystallization during extrusion. According to the literature, grain boundary precipitations (GBPs) play a critical role in localized corrosion, particularly in SCC susceptibility. The TEM results for the GBPs in each region of the extruded aluminum are displayed in Fig. 13. The grain boundaries

FIGURE 14. The MAE of literature, experimental datasets, and proposed model (a) HV model; (b) E_{corr} model.
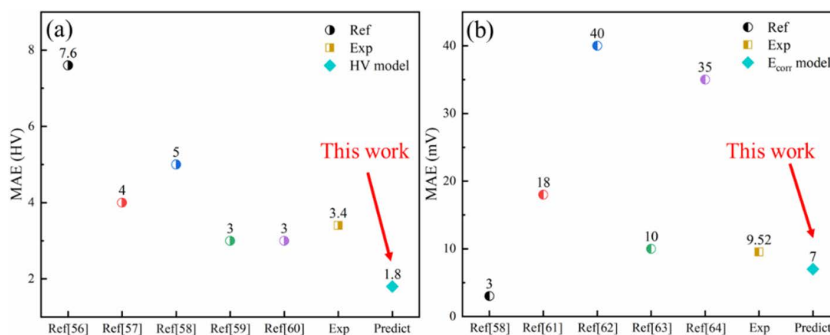
in the different regions exhibited different characteristics. From the surface to the inner region of the extruded aluminum, the number of GBPs increased and the Cu content of the GBPs decreased. In addition, the coarse grain region has a precipitate-free zone (PFZ) that is approximately 200 nm wide, while the deformed grain region has an approximately 80 nm wide PFZ, and the fine grain region possesses a 120 nm wide PFZ. As mentioned in the previous paragraph, the surface region always exhibited a higher temperature than that of the inner region. High temperatures could promote element diffusion [54], even for Cu with a high diffusion coefficient [55]. Hence, the difference in the number and Cu content of GBPs for each region in extruded aluminum is attributed to the heterogeneous temperature distribution during the extrusion process.

B. RELIABILITY OF THE PROPOSED MODELS
The deep learning model used in this study was based on a rather large dataset from the experimental results. Our results indicate that the optical microstructure of aluminum can be directly linked to HV and E_{corr}. Furthermore, the HV and E_{corr} values of a given sample can be effectively and accurately predicted using the metallographic image of the testing surface. To verify the reliability of the proposed model, the MAE between the prediction and experimental values of each model was compared with the experimental error in published literature, as shown in Fig. 14.

The experimental errors of our datasets are also presented in Fig. 14. The results demonstrated that the MAE of the HV model was lower than that of the literature and experimental results in this study. The MAE of the E_{corr} model was lower than that of the experimental results and most literature. These results demonstrate that the proposed HV and E_{corr} models can predict the HV and E_{corr} values of extruded aluminum using microstructural images with acceptable accuracy.

V. CONCLUSION
In this work, the mechanical property and corrosion behavior of large-scale extruded aluminum profiles were accurately correlated with the surface optical microstructure images by

deep learning. The relationship between the microstructure and corresponding properties were explained by EBSD, SEM, EDS and TEM analyses. The main conclusions can be summarized as below:

- The proposed model identifies the optical microstructure as the key feature that can accurately predict the HV and E_{corr} of the extruded aluminum with relatively high prediction accuracies of 90% and 82%, respectively.
- Based on the verification results, the MAE of the established HV and E_{corr} models could reach 1.8 HV and 7.0 mV, respectively.
- The main factor that affected the optical microstructure of each extruded aluminum surface and further induced the HV and E_{corr} differences was the recrystallization during the extrusion process. Specifically, full recrystallization of the surface layer softens the extruded aluminum. In addition, the low-density of the IMPs and the Cu-containing GBPs discontinuously distributed induced by recrystallization improved the corrosion resistance of extruded aluminum.

DECLARATION OF COMPETING INTEREST
The authors declare that they have no known competing financial interests or personal relationships that could have appeared to influence the work reported in this paper.

REFERENCES
[1] S. P. Knight, K. Pohl, N. J. H. Holroyd, N. Birbilis, P. A. Rometsch, B. C. Muddle, R. Goswami, and S. P. Lynch, "Some effects of alloy composition on stress corrosion cracking in Al–Zn–Mg–Cu alloys," *Corrosion Sci.*, vol. 98, pp. 50–62, Sep. 2015.

[2] S. D. Liu, Q. M. Zhong, Y. Zhang, W. J. Liu, X. M. Zhang, and Y. L. Deng, "Investigation of quench sensitivity of high strength Al–Zn–Mg–Cu alloys by time–temperature-properties diagrams," *Mater. Des.*, vol. 31, no. 6, pp. 3116–3120, Jun. 2010.

[3] S. Chen, J. Li, G.-Y. Hu, K. Chen, and L. Huang, "Effect of Zn/Mg ratios on SCC, electrochemical corrosion properties and microstructure of Al-Zn-Mg alloy," *J. Alloys Compounds*, vol. 757, pp. 259–264, Aug. 2018.

[4] W. H. Van Geertruyden, H. M. Browne, W. Z. Misiolek, and P. T. Wang, "Evolution of surface recrystallization during indirect extrusion of 6xxx aluminum alloys," *Metall. Mater. Trans. A*, vol. 36, no. 4, pp. 1049–1056, Apr. 2005.

[5] A. R. Eivani and J. Zhou, "Application of physical and numerical simulations for interpretation of peripheral coarse grain structure during hot extrusion of AA7020 aluminum alloy," *J. Alloys Compounds*, vol. 725, pp. 41–53, Nov. 2017.

[6] L. D. Pari and W. Z. Misiolek, "Theoretical predictions and experimental verification of surface grain structure evolution for AA6061 during hot rolling," *Acta Mater.*, vol. 56, no. 20, pp. 6174–6185, Dec. 2008.

[7] S. K. Kairy, S. Turk, N. Birbilis, and A. Shekhter, "The role of microstructure and microchemistry on intergranular corrosion of aluminium alloy AA7085-T7452," *Corrosion Sci.*, vol. 143, pp. 414–427, Oct. 2018.

[8] A. R. Eivani, J. Zhou, and J. Duszczyk, "Mechanism of the formation of peripheral coarse grain structure in hot extrusion of Al-4.5Zn-1Mg," *Phil. Mag.*, vol. 96, no. 12, pp. 1188–1196, Apr. 2016.

[9] Y. Zhang, S. Jin, P. W. Trimby, X. Liao, M. Y. Murashkin, R. Z. Valiev, J. Liu, J. M. Cairney, S. P. Ringer, and G. Sha, "Dynamic precipitation, segregation and strengthening of an Al-Zn-Mg-Cu alloy (AA7075) processed by high-pressure torsion," *Acta Mater.*, vol. 162, pp. 19–32, Jan. 2019.

[10] Y. Ji, C. Dong, L. Chen, K. Xiao, and X. Li, "High-throughput computing for screening the potential alloying elements of a 7xxx aluminum alloy for increasing the alloy resistance to stress corrosion cracking," *Corrosion Sci.*, vol. 183, May 2021, Art. no. 109304.

[11] Y. Sun, X. Bai, D. Klenosky, K. Trumble, and D. Johnson, "A study on peripheral grain structure evolution of an AA7050 aluminum alloy with a laboratory-scale extrusion setup," *J. Mater. Eng. Perform.*, vol. 28, no. 8, pp. 5156–5164, Aug. 2019.

[12] W. H. Van Geertruyden, W. Z. Misiolek, and P. T. Wang, "Grain structure evolution in a 6061 aluminum alloy during hot torsion," *Mater. Sci. Eng., A*, vol. 419, nos. 1–2, pp. 105–114, Mar. 2006.

[13] S. Sun, Y. Fang, L. Zhang, C. Li, and S. Hu, "Effects of aging treatment and peripheral coarse grain on the exfoliation corrosion behaviour of 2024 aluminium alloy using SR-CT," *J. Mater. Res. Technol.*, vol. 9, no. 3, pp. 3219–3229, May 2020.

[14] S. K. Li, L. X. Li, H. He, Z. W. Liu, and L. Zhang, "Influence of dynamic recrystallization on microstructure and mechanical properties of welding zone in Al–Mg–Si aluminum profile during porthole die extrusion," *Trans. Nonferrous Met. Soc. China*, vol. 29, no. 9, pp. 1803–1815, Sep. 2019.

[15] H. She, D. Shu, A. Dong, J. Wang, B. Sun, and H. Lai, "Relationship of particle stimulated nucleation, recrystallization and mechanical properties responding to Fe and Si contents in hot-extruded 7055 aluminum alloys," *J. Mater. Sci. Technol.*, vol. 35, no. 11, pp. 2570–2581, Nov. 2019.

[16] B. J. Wang, D. K. Xu, J. Sun, and E.-H. Han, "Effect of grain structure on the stress corrosion cracking (SCC) behavior of an as-extruded Mg-Zn-Zr alloy," *Corrosion Sci.*, vol. 157, pp. 347–356, Aug. 2019.

[17] M. B. Lezaack and A. Simar, "Avoiding abnormal grain growth in thick 7XXX aluminium alloy friction stir welds during T6 post heat treatments," *Mater. Sci. Eng., A*, vol. 807, Mar. 2021, Art. no. 140901.

[18] M. B. Kannan and V. S. Raja, "Enhancing stress corrosion cracking resistance in Al–Zn–Mg–Cu–Zr alloy through inhibiting recrystallization," *Eng. Fract. Mech.*, vol. 77, no. 2, pp. 249–256, Jan. 2010.

[19] S. P. Knight, N. Birbilis, B. C. Muddle, A. R. Trueman, and S. P. Lynch, "Correlations between intergranular stress corrosion cracking, grain-boundary microchemistry, and grain-boundary electrochemistry for Al–Zn–Mg–Cu alloys," *Corrosion Sci.*, vol. 52, no. 12, pp. 4073–4080, Dec. 2010.

[20] S. Lei, W. Jiu-Ba, and R. Chang, "The prediction of microstructure evolution of 6005A aluminum alloy in a P-ECAP extrusion study," *J. Mater. Eng. Perform.*, vol. 27, no. 5, pp. 2566–2575, May 2018.

[21] A. Güzel, A. Jäger, F. Parvizian, H.-G. Lambers, A. E. Tekkaya, B. Svendsen, and H. J. Maier, "A new method for determining dynamic grain structure evolution during hot aluminum extrusion," *J. Mater. Process. Technol.*, vol. 212, no. 1, pp. 323–330, Jan. 2012.

[22] Y. Z. Ning and C. Q. Sun, "Study on the Coarse and Fine Grains of Aluminum Alloys LY12CZ," *Mater. Mech. Eng.*, vol. 4, pp. 39–43, Aug. 1992.

[23] Z. C. Sun, L. S. Zheng, and H. Yang, "Softening mechanism and microstructure evolution of as-extruded 7075 aluminum alloy during hot deformation," *Mater. Characterization*, vol. 90, pp. 71–80, Apr. 2014.

[24] L. Y. Ye, X. B. Yao, H. Q. Lin, S. D. Liu, Y. L. Deng, and X. M. Zhang, "Coarse grain layer on stress corrosion cracking resistance of Al–Zn–Mg Alloy," in *Proc. Chin. Mater. Conf.*, Singapore, 2018, pp. 337–347.

[25] X. Zhang, X. Zhou, J.-O. Nilsson, Z. Dong, and C. Cai, "Corrosion behaviour of AA6082 Al-Mg-Si alloy extrusion: Recrystallized and non-recrystallized structures," *Corrosion Sci.*, vol. 144, pp. 163–171, Nov. 2018.

[26] J. Wloka, T. Hack, and S. Virtanen, "Influence of temper and surface condition on the exfoliation behaviour of high strength Al–Zn–Mg–Cu alloys," *Corrosion Sci.*, vol. 49, no. 3, pp. 1437–1449, Mar. 2007.

[27] M. Ao, C. Dong, N. Li, L. Wang, Y. Ji, L. Yue, X. Sun, S. Zou, K. Xiao, and X. Li, "Unexpected stress corrosion cracking improvement achieved by recrystallized layer in Al-Zn-Mg alloy," *J. Mater. Eng. Perform.*, vol. 30, no. 8, pp. 6258–6268, Aug. 2021.

[28] Y. Z. Xu, J. Y. Li, M. F. Qi, J. B. Gu, and Y. Zhang, "Effect of extrusion on the microstructure and corrosion behaviors of biodegradable Mg–Zn–Y–Gd–Zr alloy," *J. Mater. Sci.*, vol. 55, no. 3, pp. 1231–1245, Jan. 2020.

[29] C. Duan, J. Tang, W. Ma, L. Ye, H. Jiang, Y. Deng, and X. Zhang, "Intergranular corrosion behavior of extruded 6005A alloy profile with different microstructures," *J. Mater. Sci.*, vol. 55, no. 24, pp. 10833–10848, Aug. 2020.

[30] A. Krizhevsky, I. Sutskever, and G. E. Hinton, "Imagenet classification with deep convolutional neural networks," in *Proc. Adv. Neural Inf. Process. Syst.*, Las Vegas, NV, USA, 2012, pp. 1097–1105.

[31] C. Dong, C. C. Loy, K. He, and X. Tang, "Image super-resolution using deep convolutional networks," *IEEE Trans. Pattern Anal. Mach. Intell.*, vol. 38, no. 2, pp. 295–307, Feb. 2016.

[32] D. Zhang, J. Lv, and Z. Cheng, "An approach focusing on the convolutional layer characteristics of the VGG network for vehicle tracking," *IEEE Access*, vol. 8, pp. 112827–112839, 2020.

[33] J. Ni, J. Gao, L. Deng, and Z. Han, "Monitoring the change process of banana freshness by GoogLeNet," *IEEE Access*, vol. 8, pp. 228369–228376, 2020.

[34] B. Li and Y. He, "An improved ResNet based on the adjustable shortcut connections," *IEEE Access*, vol. 6, pp. 18967–18974, 2018.

[35] S. Ren, K. He, R. Girshick, and J. Sun, "Faster R-CNN: Towards real-time object detection with region proposal networks," in *Adv. Neural Inf. Process. Syst.; Neural Inf. Process. Syst.*, San Diego, CA, USA, 2015, pp. 91–99.

[36] G. Huang, Z. Liu, L. van der Maaten, and K. Q. Weinberger, "Densely connected convolutional networks," in *Proc. IEEE Conf. Comput. Vis. Pattern Recognit.*, Honolulu, HI, USA, Jul. 2017, pp. 2261–2269.

[37] T. Fujioka, M. Mori, K. Kubota, Y. Kikuchi, L. Katsuta, M. Adachi, G. Oda, T. Nakagawa, Y. Kitazume, and U. Tateishi, "Breast ultrasound image synthesis using deep convolutional generative adversarial networks," *Diagnostics*, vol. 9, no. 4, p. 176, Nov. 2019.

[38] K. Zhang et al., "Deep-learning models for the detection and incidence prediction of chronic kidney disease and type 2 diabetes from retinal fundus images," *Nature Biomed. Eng.*, vol. 5, no. 6, pp. 533–545, Jun. 2021.

[39] H. Zhang, H. Fu, S. Zhu, W. Yong, and J. Xie, "Machine learning assisted composition effective design for precipitation strengthened copper alloys," *Acta Mater.*, vol. 215, Aug. 2021, Art. no. 117118.

[40] B. Ma, X. Ban, H. Huang, Y. Chen, W. Liu, and Y. Zhi, "Deep learning-based image segmentation for Al-La alloy microscopic images," *Symmetry*, vol. 10, no. 4, p. 107, Apr. 2018.

[41] B. Ma, X. Wei, C. Liu, X. Ban, H. Huang, H. Wang, W. Xue, S. Wu, M. Gao, Q. Shen, M. Mukeshimana, A. O. Abuassba, H. Shen, and Y. Su, "Data augmentation in microscopic images for material data mining," *npj Comput. Mater.*, vol. 6, no. 1, p. 125, Aug. 2020.

[42] J. Na, G. Kim, S.-H. Kang, S.-J. Kim, and S. Lee, "Deep learning-based discriminative refocusing of scanning electron microscopy images for materials science," *Acta Mater.*, vol. 214, Aug. 2021, Art. no. 116987.

[43] K. Simonyan and A. Zisserman, "Very deep convolutional networks for large-scale image recognition," in *Proc. Int. Conf. Learn. Represent.*, San Diego, CA, USA, 2015.

[44] C. Szegedy, W. Liu, Y. Jia, P. Sermanet, S. Reed, D. Anguelov, D. Erhan, V. Vanhoucke, and A. Rabinovich, "Going deeper with convolutions," in *Proc. IEEE Comput. Soc. Conf. Comput. Vis. Pattern Recognit.*, Boston, MA, USA, Jun. 2015, pp. 1–9.

[45] K. He, X. Zhang, S. Ren, and J. Sun, "Deep residual learning for image recognition," in *Proc. IEEE Conf. Comput. Vis. Pattern Recognit. (CVPR)*, Las Vegas, NV, USA, Jun. 2016, pp. 770–778.

[46] C. Szegedy, V. Vanhoucke, S. Ioffe, J. Shlens, and Z. Wojna, "Rethinking the inception architecture for computer vision," in *Proc. IEEE Conf. Comput. Vis. Pattern Recognit. (CVPR)*, Las Vegas, NV, USA, Jun. 2016, pp. 2818–2826.

[47] C. Szegedy, S. Ioffe, and V. Vanhoucke, "Inception-V4, inception-resnet and the impact of residual connections on learning," in *Proc. AAAI Conf. Artif. Intell.*, San Francisco, CA, USA, Feb. 2017, pp. 4278–4284.

[48] A. Ziletti, D. Kumar, M. Scheffler, and L. M. Ghiringhelli, "Insightful classification of crystal structures using deep learning," *Nature Commun.*, vol. 9, no. 1, p. 2775, Jul. 2018.

[49] H. C. Ma, Z. Y. Liu, C. W. Du, H. R. Wang, X. G. Li, D. W. Zhang, and Z. Y. Cui, "Stress corrosion cracking of E690 steel as a welded joint in a simulated marine atmosphere containing sulphur dioxide," *Corrosion Sci.*, vol. 100, pp. 627–641, Nov. 2015.

[50] Y. Takayama, E. Harunari, and H. Kato, "Change in crystallographic orientation distribution during high temperature deformation in an Al-Mg-Mn alloy sheet consisting of coarse- and fine-grained layers," *Mater. Trans.*, vol. 45, no. 8, pp. 2525–2530, 2004.

[51] J. X. Xie and J. N. Liu, *Theory and Technology of Metals Extrusion*, 2nd ed. Beijing, China: Metallurgical Industry Press, 2012.

[52] A. Yanagida, J. Liu, and J. Yanagimoto, "Flow curve determination for metal under dynamic recrystallization using inverse analysis," *Mater. Trans.*, vol. 44, no. 11, pp. 2303–2310, 2003.

[53] S. Gourdet and F. Montheillet, "An experimental study of the recrystallization mechanism during hot deformation of aluminium," *Mater. Sci. Eng., A*, vol. 283, nos. 1–2, pp. 274–288, May 2000.

[54] A. C. U. Rao, V. Vasu, M. Govindaraju, and K. V. S. Srinadh, "Stress corrosion cracking behaviour of 7xxx aluminum alloys: A literature review," *Trans. Nonferrous Met. Soc. China*, vol. 26, no. 6, pp. 1447–1471, Jun. 2016.

[55] R. Goswami, S. Lynch, N. J. H. Holroyd, S. P. Knight, and R. L. Holtz, "Evolution of grain boundary precipitates in al 7075 upon aging and correlation with stress corrosion cracking behavior," *Metall. Mater. Trans. A*, vol. 44, no. 3, pp. 1268–1278, Mar. 2013.

[56] S. Ngai, T. Ngai, F. Vogel, W. Story, G. B. Thompson, and L. N. Brewer, "Saltwater corrosion behavior of cold sprayed AA7075 aluminum alloy coatings," *Corrosion Sci.*, vol. 130, pp. 231–240, Jan. 2018.

[57] M. Karamouz, M. Azarbarmas, M. Emamy, and M. Alipour, "Microstructure, hardness and tensile properties of A380 aluminum alloy with and without li additions," *Mater. Sci. Eng., A*, vol. 582, pp. 409–414, Oct. 2013.

[58] Y. Wang, L. Cao, X. Wu, X. Tong, B. Liao, G. Huang, and Z. Wang, "Effect of retrogression treatments on microstructure, hardness and corrosion behaviors of aluminum alloy 7085," *J. Alloys Compounds*, vol. 814, Jan. 2020, Art. no. 152264.

[59] K. Tahmasbi, M. Mahmoodi, and H. Tavakoli, "Corrosion resistance of aluminum alloy AA7022 wire fabricated by friction stir extrusion," *Trans. Nonferrous Met. Soc. China*, vol. 29, no. 8, pp. 1601–1609, Aug. 2019.

[60] X. W. Yu, J. H. Chen, J. Y. Li, C. L. Wu, and X. B. Yang, "Effect of pre-deformation on quench-induced inhomogeneity of microstructure and hardness in 7050 aluminum alloy," *Mater. Characterization*, vol. 158, Dec. 2019, Art. no. 110005.

[61] J. Wang, F. Xiong, H. Liu, T. Zhang, Y. Li, C. Li, W. Xia, H. Wang, and H. Liu, "Study of the corrosion behavior of aspergillus Niger on 7075-T6 aluminum alloy in a high salinity environment," *Bioelectrochemistry*, vol. 129, pp. 10–17, Oct. 2019.

[62] W. Xiao and Y. Wang, "Corrosion resistance of aluminum fluoride modified 6061 aluminum alloy," *Mater. Lett.*, vol. 298, Sep. 2021, Art. no. 129932.

[63] P. Fathi, M. Rafieazad, E. Mohseni-Sohi, M. Sanjari, H. Pirgazi, B. Shalchi Amirkhiz, A. Nasiri, and M. Mohammadi, "Corrosion performance of additively manufactured bimetallic aluminum alloys," *Electrochim. Acta*, vol. 389, Sep. 2021, Art. no. 138689.

[64] D. S. Kharitonov, I. Dobryden, B. Sefer, J. Ryl, A. Wrzesińska, I. V. Makarova, I. Bobowska, I. I. Kurilo, and P. M. Claesson, "Surface and corrosion properties of AA6063-T5 aluminum alloy in molybdate-containing sodium chloride solutions," *Corrosion Sci.*, vol. 171, Jul. 2020, Art. no. 108658.

MIN AO is currently pursuing the Ph.D. degree with the University of Science and Technology Beijing. Her research interests include integrated calculation of metal corrosion and deep learning.

YUCHENG JI is currently pursuing the Ph.D. degree with the University of Science and Technology Beijing. His research interests include force on the Al corrosion mechanism explore and corrosion resistance structure design based on materials genetic engineering.

XIAOGUANG SUN is currently a Professor at the Technical Engineering Department, CRRC Qingdao Sifang Company Ltd. His research interests include surface engineering, remanufacturing, corrosion, and protection of railway equipments.

FENGJIA GUO is currently an intermediate Engineer at Shandong Nanshan Aluminium Company Ltd. His research interests include performance optimization and characterization of metal materials.

KUI XIAO is currently a Professor and the Doctoral Supervisor at the University of Science and Technology Beijing. His research interests include atmospheric corrosion behavior and mechanism of metallic materials.

CHAOFANG DONG is currently a Professor and the Doctoral Supervisor at the University of Science and Technology Beijing. Her research interests include integrated calculation of metal corrosion and designs corrosion-resistant materials.

• • •